Two-dimensional simulation on the micro-floating zone of laser-heated pedestal growth using the control-volume finite difference method

P. Y. Chen[1*], C. L. Chang [2], C. W. Lan[3], and S. L. Huang[24]

[1]Department of Gemology, Meiho Institute of Technology, Pingtung 91202, Taiwan
[2]Institute of Photonic & Optoelectronics, National Taiwan University, Taipei 10617, Taiwan
[3]Department of Chemical Engineering, National Taiwan University, Taipei 10617, Taiwan
[4]Department of Electrical Engineering, National Taiwan University, Taipei 10617, Taiwan

Abstract

A two-dimensional simulation was employed to study the melt/air and melt/solid interface shapes of the miniature molten zone formed in the laser-heated pedestal growth (LHPG) system. Using non-orthogonal body-fitting grid system with control-volume finite difference method, the interface shape can be determined both efficiently and accurately. During stable growth, the dependence of the molten-zone length and shape on the heating CO_2 laser is examined in detail under both the maximum and the minimum allowed powers with various growth speeds. The effect of gravity for the miniature molten zone is also simulated, which reveals the possibility for a horizontally oriented LHPG system.

After comparing with the shape of the molten zone in terms of the experiment and the analysis of the simulation shown as above. Heat transfer and fluid flow in the LHPG system are analyzed near the deformed interfaces. The global thermal distributions of the crystal fiber, the melt, and the source rod are described by temperature and its axial gradient within length of ~10 mm. As compared with the growth of bulk crystal of several centimeters in dimension, natural convection drops six orders in magnitude due to smaller melt volume; therefore, conduction rather than convection determines the temperature distribution in the molten zone. Moreover, thermocapillary convection rather than mass-transfer convection becomes dominant. The symmetry and mass flow rate of double eddy pattern are significantly influenced by the molten-zone shape due to the diameter reduction and the large surface-tension-temperature coefficient in the order of 10^{-4}~10^{-3}. According to the analysis shown as above, the results could be further extended for the analysis of the concentration profile and study of horizontal growth.

Keyword: Interface shape, laser-heated pedestal growth, YAG, single-crystal fiber, heat transfer, fluid flow

利用有限體積差分法於雷射基座加熱生長的微浮動熔區之二維模擬

陳平夷 [1*], 張俊霖 [2], 藍崇文 [3],黃升龍 [24]

[1] 美和技術學院珠寶技術系
[2] 國立台灣大學光電工程研究所
[3] 國立台灣大學化學工程學系
[4] 國立台灣大學電機工程學系

摘 要

本論文以二維模擬於雷射基座加熱生長(Laser-heated pedestal growth; LHPG) 系統之微浮動熔區氣液與固液介面形狀的研究，數值方法係使用有限體積差分方法(control-volume finite difference method)之非正交體適網格系統(non-orthogonal body-fitting grid system)，使得介面形狀能夠被有效率與精準測定。在穩定長晶情況下，各種長晶速度的熔區在 CO_2 雷射加熱下，其所允許最高與最低加熱功率的熔區長度和形狀能夠被詳細檢測出來，並且重力對微浮動熔區的效應也被模擬分析，它顯示水平生長方向 LHPG 的可能性，此水平系統將有利於長晶纖的生長操作。

以上熔區形狀的實驗與模擬分析比對後，對於 LHPG 的熔區之熱傳(heat transfer)與流體流動(fluid flow)作了分析，在長度尺度約為一公分的系統中，完整的描述了包含原棒與熔區以及晶纖所組成的全域溫度與軸向溫度梯度。當比較原棒直徑尺度約為幾公分大之塊材的長晶系統時，較小的尺度熔區內，自然對流(natural convection)強度將下降約六個數量級。因而是熱傳導決定了熔區內的溫度分布而不是熱對流效應。對流呈現由熱毛細對流(thermocapillary convection)與質傳對流(mass-transfer convection)主控，而且熱毛細對流強度最後演化也變得比質傳對流大，主控了熔區內流場分布。當熱毛細對流係數大到約為 10^{-4}~10^{-3} 時，熔區的形狀呈現對稱與雙渦流分佈，因縮徑對熔區內流場所造成的影響是非常小的。經由以上的分析，其結果將可更進一步提供爾後濃度分析與水平生長製程之基礎。

關鍵字：介面形狀, 雷射基座加熱生長, 石榴石, 晶體光纖, 熱傳, 流場

1. Introduction

Single-crystal fibers have become the subject of intense study recently. They have been recognized to possess remarkable characteristics. Some applications for passive devices [1] and active devices [2-4] have been made in our group. Laser-heated pedestal growth (LHPG) method [5,6] are the crucible-free technique with the main advantages including high pulling rates, low production cost, and the feasibility of growing materials with very high melting points, high purity and low stress.

For growing high-quality crystal fibers, the stability of the molten zone can be revealed by its specific interface shape during the growth process. How to describe it accurately by theories or experiments has been the subject of studies for many years. For the miniature molten zone fabricated using the LHPG method, the variation in pressure induced by the stable convections can be expressed by the shape, volume and stability of the melt at various laser powers. For bulk crystal growth using the floating-zone method, a non-orthogonal body-fitting grid system [7] has

*Associate professor at Department of Gemology in Meiho Institute of Technology
(E-mail:x00008415@meiho.edu.tw;TEL:+886-8-7799821-6506)

been successfully employed to predict more accurately the interface shapes.

In order to describe the growth of a single-crystal fiber using the LHPG method, several numerical models have been used. However, there is still no accurate simulation model for describing these deformed interface shapes of the miniature molten zone. In this paper, we report a two-dimensional simulation results and its experimental verification [8]. The numerical model is modified from that for growing bulk crystals using the floating-zone method [9]. Using a non-orthogonal body-fitting grid system [7] with the control-volume finite-difference method [10], it is possible to obtain more accurate estimations near the interface in order to reduce the computation time. Moreover, the laser intensity profile and boundary conditions are revised because the heat source is replaced by a carbon dioxide (CO_2) laser.

For the miniature molten zone (MZ) fabricated using the LHPG method, there are three kinds of thermal convections. The buoyancy-driven natural convection is influenced by melt volume, viscosity, and the variation of the temperature-dependent localized melt density. The thermocapillary (TC) convection is originated from the variation of surface tension, which is a function of temperature and concentration [11]. The mass-transfer convection as convective transport is determined by the growth and feed speeds. In this paper, we report in detail the heat transfer and fluid flow in the LHPG system to visualize the intermediate phenomena which cannot be observed easily from experiments [12]. How the stream function pattern and the temperature distribution can be influenced is discussed and then the contributions of individual convections are analyzed.

2. Mathematical formulation

Figure 1 (a) illustrates the LHPG method [8,13] for growing SCFs. A 100-W, 10.6-μm CO_2 laser system was the heat source to enter the growth chamber. Inside the chamber, the incident Gaussian laser beam was transformed into a ring-shaped semi-Gaussian beam by the reflaxicon. The ring-shaped beam was reflected by a planar mirror, and then focused by a parabolic mirror to form a highly-concentrated heat zone on the melt. The source rods were cut from yttrium aluminum garnet (YAG) crystals in <111> direction.

Figure 1 (b) illustrates the miniature MZ in the LHPG system. The ambient temperature is constant. Thermal convection is symmetric axially, laminar at a pseudo-steady state. The oscillation of thermocapillary convection is neglected. Furthermore, gravity and 2D cylindrical coordinate are considered. Three governing equations are listed below:

Equation of motion,

$$\frac{\partial}{\partial r}\left(\frac{\omega}{r}\frac{\partial \psi}{\partial z}\right)-\frac{\partial}{\partial z}\left(\frac{\omega}{r}\frac{\partial \psi}{\partial r}\right)+ \frac{\partial}{\partial r}\left[\frac{1}{r}\frac{\partial}{\partial r}\left(\mu_{\mathrm{m}} r\omega\right)\right]+\frac{\partial}{\partial z}\left[\frac{1}{r}\frac{\partial}{\partial r}\left(\mu_{\mathrm{m}} r\omega\right)\right]-\rho_{\mathrm{m}}\beta_{\mathrm{m}} g\frac{\partial T}{\partial r}=0. \quad (1)$$

Stream function,

$$\frac{\partial}{\partial z}\left(\frac{1}{\rho_{\mathrm{m}} r}\frac{\partial \psi}{\partial z}\right)+\frac{\partial}{\partial r}\left(\frac{1}{\rho_{\mathrm{m}} r}\frac{\partial \psi}{\partial r}\right)+\omega=0. \quad (2)$$

Energy function,

$$\frac{\partial}{\partial r}\left(C_{\mathrm{pm}} T\frac{\partial \psi}{\partial z}\right)-\frac{\partial}{\partial z}\left(C_{\mathrm{pm}} T\frac{\partial \psi}{\partial r}\right)+ \frac{\partial}{\partial z}\left(rk_{\mathrm{s,m}}\frac{\partial T}{\partial z}\right)+\frac{\partial}{\partial r}\left(rk_{\mathrm{s,m}}\frac{\partial T}{\partial r}\right)=0. \quad (3)$$

where ψ, ω, μ_{m}, ρ_{m}, β_{m}, C_{pm}, T, and $k_{\mathrm{s,m}}$ are the stream function (g s^{-1}), vorticity, viscosity of melt, density of melt, thermal expansion coefficient of melt, specific heat of melt, temperature, and thermal conductivity of solid or melt, respectively. Moreover, the radial velocity, axial velocity, and vorticity are u, υ, and ω, respectively:

$$u=-\frac{1}{\rho_{\mathrm{L}} r}\frac{\partial \psi}{\partial z},\upsilon=\frac{1}{\rho_{\mathrm{L}} r}\frac{\partial \psi}{\partial r},\omega\equiv\frac{\partial u}{\partial z}-\frac{\partial \upsilon}{\partial r}. \quad (4)$$

Three thermal and fluid boundary conditions are (1) along z axis, (2) at the melt/solid interface, and (3) on the surfaces of the source rod, the melt, and the crystal fiber. There is additional thermal condition far away from the melt. The laser intensity profile on the miniature MZ is an asymmetrical Gaussian distribution,

$$I_{\mathrm{a}}=A_{\mathrm{q}}\exp\left[-\alpha_{\mathrm{a}}(z/\gamma_{\mathrm{a}})^2\right]. \quad (5)$$

where A_{q} and γ_{a} are the amplitude and Gaussian width ($1/e^2$) at z = 0, and α_{a} is the beam-shape factor.

3. Result and discussion

3.1 Comparison between experiments and simulations

Figure 2 shows a comparison between experiments and simulations on the molten-zone lengths at various laser powers for different reduction ratios. The source rod size is 300 μm and the feed speed is 1.2 mm per minute. The reduction ratios are 100%, 35%, and 25% for (a), (b), and (c), respectively. When normalized to the source-rod diameter, the allowed molten-zone lengths are 1.07-1.53 in (a), 1.07-1.72 in (b), and 0.67-1.46 in (c). By decreasing the reduction ratios, the allowed laser power is lower. We are also aware that the maximum length of the molten zone divided by the minimum length is 2±0.5 for stable growth. Similar

empirical criteria have been introduced previously. The contact angle at the tri-point and the surface tension depend on the ability of the material to restrict variations in the melt/air interface shape. For fixed contact angle, the shapes of the melt/air interface and the molten-zone length can be varied by changing the laser power or reduction ratios. The upper melt/solid interface is more convex toward the melt can be obtained at lower growth speed and is determined by both the temperature gradient normal to the melt/solid interface and the release of the latent heat.

Figure 3 (a) shows η at various reduction ratios for different feed speeds with the reduction ratio of 35%. If the feed and growth speeds are zero, the heat energy is stored in the melt, and this situation results in the largest value of η for a reduction ratio of less than 70%. With the same source rod and feed speed, the increase in η becomes saturated by decreasing the reduction ratio, because the cross section at the melt/solid interface becomes smaller. The parabolic trend of η indicates that is inversely proportional to the cross section of the upper melt/solid interface. By increasing the feed speed, η decreases at a reduction ratio of less than 70% but increases at a higher reduction ratio using the same source rod. The reason is that heat removal via mass-transfer
convection is enhanced by increasing the feed speed at the lower reduction ratios. However, there is a trade-off between the mass transfer and the cross section at the melt/solid interface due to continuity. When increasing the feed speed, η becomes higher owing to the larger cross section at the melt/solid interface.

Figure 3 (b) shows the radial positions of the melt/air interface and the curvature radius at various axial positions with the reduction ratio of 35%. An inflection point can be identified by the peak value of the curvature radius at various axial positions. The melt/air interface is wine-bottle shaped. The higher peak value of the curvature radius means a smoother profile at the inflection point. Moreover, the axial position of the inflection point reveals the degree to which the molten zone extends radially at the bottom. The inflection point moves from 'z < 0' to 'z > 0' and the peak value of the curvature radius decreases as the laser power rises. The laser heating efficiency for the same melt volume can be improved if the laser beam is projected onto the position (z=0) near the location of the peak curvature radius.

Figure 3 (c) simulates the effect of gravity on the melt/air interface with the reduction ratio of 35%. There is almost no difference between normal and near-zero gravity. At H_C, surface tension shows an observable reduction in molten-zone length with near-zero gravity. The variation in the length of the molten zone due to gravity is much smaller than that effected by varying the laser power. Therefore, a variation in gravity along the growth direction will not obviously affect the stable conditions for growing crystal fibers.

3.2 Analysis of heat flow in the molten zone

Figure 4 shows T and dT/dz near the miniature MZ at various axial positions for different reduction ratios when operating at high (H) and low (L) allowed laser power in the figure 2. Where H_a, H_b, and H_c are 6.7 W, 2.2 W, 1.68 W, and 1.5 W. L_a, L_b, and L_c are 5.5 W, 2.05 W, 1.55 W, and 1.3 W. They represent the range of input laser powers for stable growth of crystal fibers. The dT/dz reaches the maximum before the melt/solid interfaces because there is space for thermal flux to make a turn from radial to axial direction. As the reduction ratio decreases, the dT/dz distribution along z axis is closer to that along the melt/air interface. The growth/feed fronts can also be precisely identified by observing the local extremes of dT/dz due to the release/absorption of the latent heat. The differences in area under the curves of temperature distribution are smaller as the reduction ratio decreases because more internal energies stay near the z axis in the melt. The upper diagrams are corresponding streamlines and isotherms of the miniature MZ. The patterns of the double eddy flow are almost symmetric when the reduction ratio is 100%. The temperature distribution is not influenced by fluid flow significantly because conduction is dominant rather than convection and radiation due to the small melt volume.

In static MZ ($U_{s,c} = 0$) without TC convection, only natural convection is formed with single eddy. The strongest mass flow rate is in the order of 10^{-9} g/s in the loop center and the peak temperature is about 2378 K. Figure 5 (a) shows the streamlines and isotherms for different $\partial\gamma/\partial T$ with the reduction ratio of 35%. The natural convection cannot be observed because its mass flow rate drops six orders in magnitude due to the miniature volume of MZ. The TC convection becomes stronger as $\partial\gamma/\partial T$ is increased. The stable double eddies are formed when the mass flow rate reaches the order of 10^{-6}~10^{-5} g s^{-1}. For YAG, $\partial\gamma/\partial T$ is -3.5×10^{-2} dyn cm^{-1} K^{-1} [14] and the resulting magnitude of mass flow rate are in the order of 10^{-5}~10^{-4} g s^{-1}, which is comparable to that in FZ bulk crystal growth. The TC convection are in similar order because there is higher heat density using laser heating method, but

smaller total melt/air interface area. Although the growth speed is much slower during the bulk crystal growth, the mass flow rate is still larger than that during the LHPG SCFs growth. In term of the induced mass flow rate among the three convections, TC ≥ mass-transfer >> natural is the typical behavior during the LHPG SCFs growth. Typically the lower eddy is formed faster than the upper one.

Figure 5 (b) shows the shapes of the melt/air interface with the reduction ratio of 35% by considering different kinds of thermal convections. At H_c, the discrepancy between curves 1~3 can clearly be observed. This is mainly due to the larger MZ volume and melt/air interface area for stronger mass-transfer and TC convections. At L_c, there is almost no difference between curves 4 and 5. For curve 6, the melt/air interface slightly becomes more convex outward due to the enhancement of the TC convection near the melt/air interface.

4.Conclusion

A two-dimensional simulation on the miniature molten zone fabricated using the LHPG method for growing single-crystal fibers was successfully modified from that for growing bulk crystals using the floating-zone method. The stable conditions utilized for producing a useful crystal fiber are defined. The effects caused by thermocapillary and mass-transfer convection in the melt and the trade-off between mass transfer and cross section at the melt/solid interface for heat dissipation are discussed. The melt/air interface is estimated and optimized for efficient laser absorption according to curvature radius and the inflection point. There is no significant change if the gravity is varied along the growth direction. The influence of gravity is discussed with reference to the feasibility of growing a crystal fiber horizontally.

Finally, heat transfer and fluid flow in the LHPG system are analyzed. Due to the small melt volume in the LHPG system, natural convection drops six orders in magnitude from several centimeters to hundred microns in dimension; therefore conduction rather than convection dominates the temperature distribution. TC convection rather than mass-transfer convection becomes dominant for large mass flow rate in the melt. Based on this work, the dopant concentration profile of the grown crystal fiber for active devices can be investigated further.

Acknowledgements

The authors gratefully acknowledge the support for this work in part by the National Science Council, Republic of China under contract number NSC 96-2628-E-002-042-MY3.

References

[1] C. N. Tsai, Y. S. Lin, K. Y. Huang , Y. S. Lin, C. C. Lai, and S. L. Huang, Jpn. J. Appl. Phys. vol. 47, pp. 6369-6373, 2008.
[2] C. C. Lai, K. Y. Huang, H. J. Tsai, K. Y. Hsu, S. K. Liu, C. T. Cheng, K. D. Ji, C. P. Ke, S. R. Lin, and S. L. Huang, Opt. Lett. vol. 34, pp. 2357-2359, 2009.
[3] K. Y. Huang, K. Y. Hsu, and S. L. Huang, IEEE Lightwave Technol. vol. 26, pp. 1632-1639, 2008.
[4] L. M. Lee, S. C. Pei, D. F. Lin, M. C. Tsai, T. M. Tai, P. C. Chiu, D. H. Sun, A. H. Kung, and S. L. Huang, J. Opt. Soc. Am. B vol. 24, pp. 1909-1915, 2007.
[5] M. M. Fejer, J. L. Nightingale, G. A. Magel, and R. L. Byer, Rev. Sci. Instrum. vol. **55**, pp. 1791-1796, 1984.
[6] R. S. Feigelson, J. Cryst. Growth vol. 79, pp. 669-680, 1986.
[7] J. F. Thompson, F. C. Thames, and C. W. Mastin, J. Comp. Phys. vol. 15, pp. 299-319, 1974.
[8] P. Y. Chen, C. L. Chang, K. Y. Huang, C. W. Lan, W. H. Cheng, and S. L. Huang, J. Appl. Cryst. vol. 42, pp. 553-563, 2009.
[9] C. W. Lan and S. Kou, J. Cryst. Growth vol.108, pp.351-366, 1991.
[10] C. W Lan and S. Kou, Intern. J. Numer. Methods Fluids vol. 12, pp. 59-80, 1991.
[11] N. Kobayashi: Jpn. J. Appl. Phys. vol. 27, pp.20-24, 1988.
[12] P. Y. Chen, C. L. Chang, C. W. Lan, W. H. Cheng, and S. L. Huang, Jpn. J. Appl. Phys., vol. 48, pp.115504, 2009.
[13] K. Y. Huang, K. Y. Hsu, D. Y. Jheng, W. J. Zhuo, P. Y. Chen, P. S. Yeh, and S. L. Huang, Opt. Express vol.16, pp. 12264-12271, 2008.
[14] V. J. Fratello and C. D. Brandle, J. Cryst. Growth vol. 128, pp. 1006-1010, 1993.

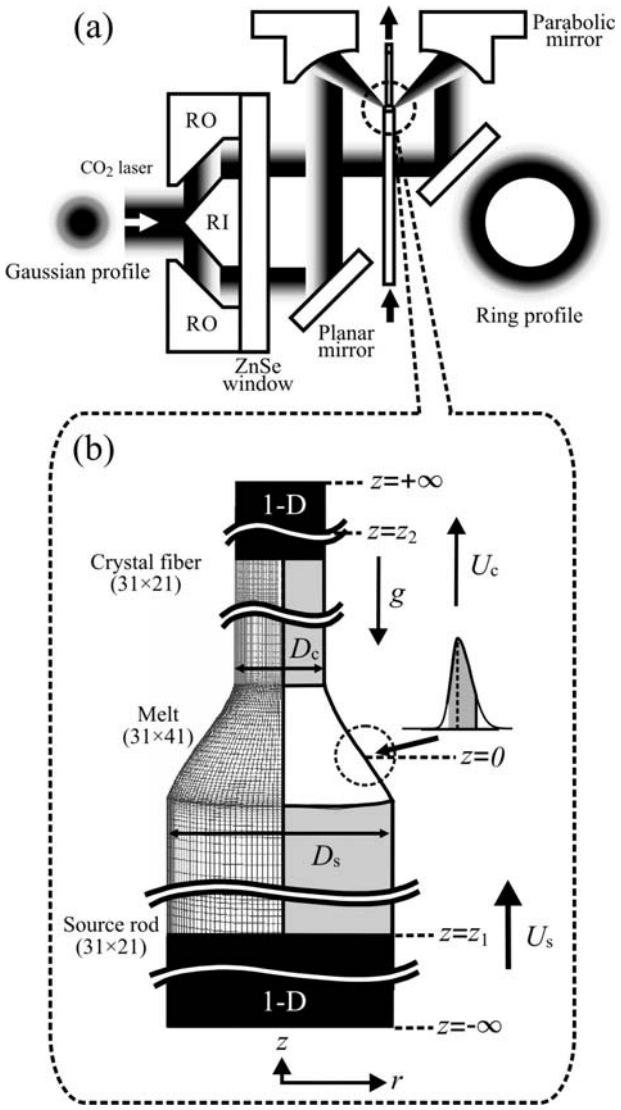

FIG. 1. (a) The illustration of the LHPG SCFs growth. RO and RI are the outer-cone and inner-cone reflaxicon; (b) The miniature MZ in the curvilinear coordinate for the physical domain (left) and the sketch (right).

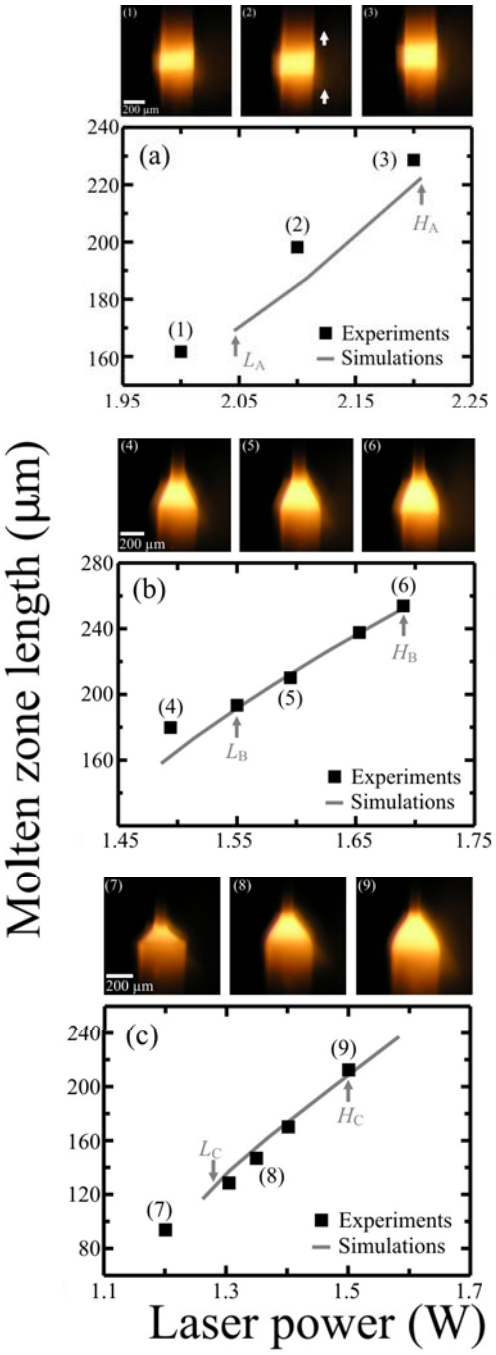

FIG. 2. Miniature molten-zone lengths at various laser powers for different reduction ratios in both experiments and simulations. The gray arrows labeled *H* and *L* are the higher and lower allowed laser powers. The upper indexed captured images of the miniature molten zones correspond to those in Fig. 2.

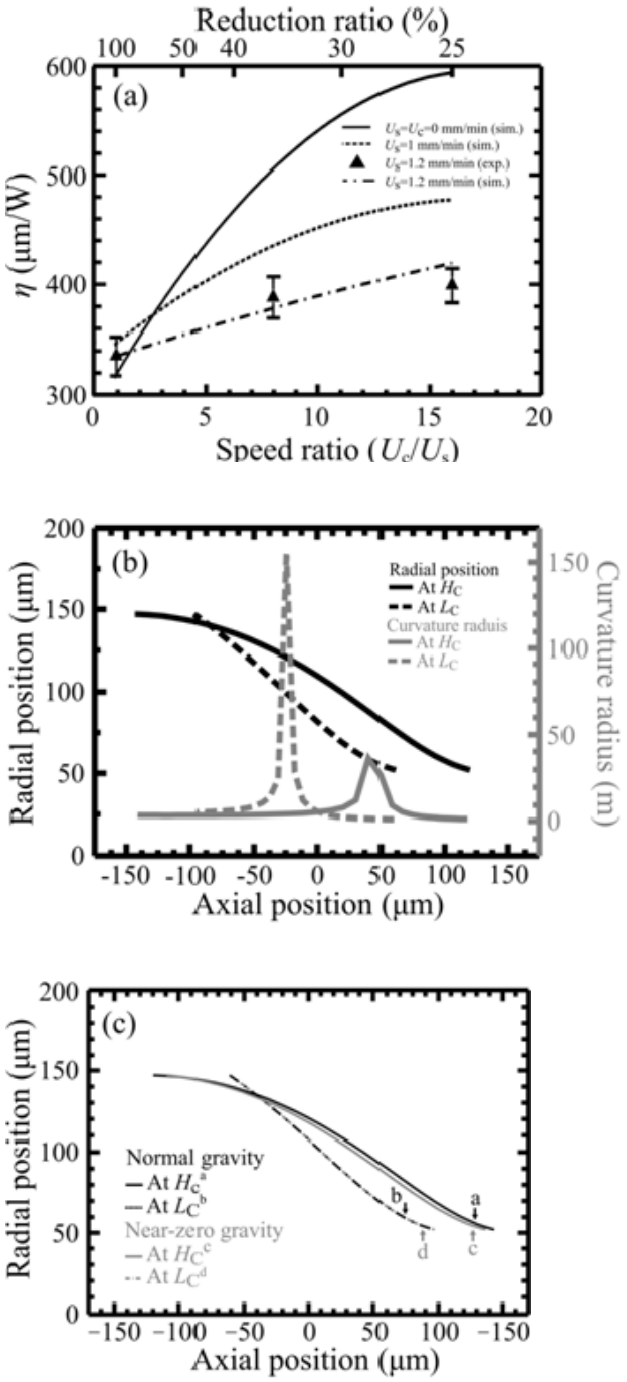

FIG. 3 (a) The slopes η at various reduction ratios for different feed speeds. (b) The radial positions and the curvature radius of the melt/air interface at various axial positions. (c) The radial positions of the melt/air interface at various axial positions.

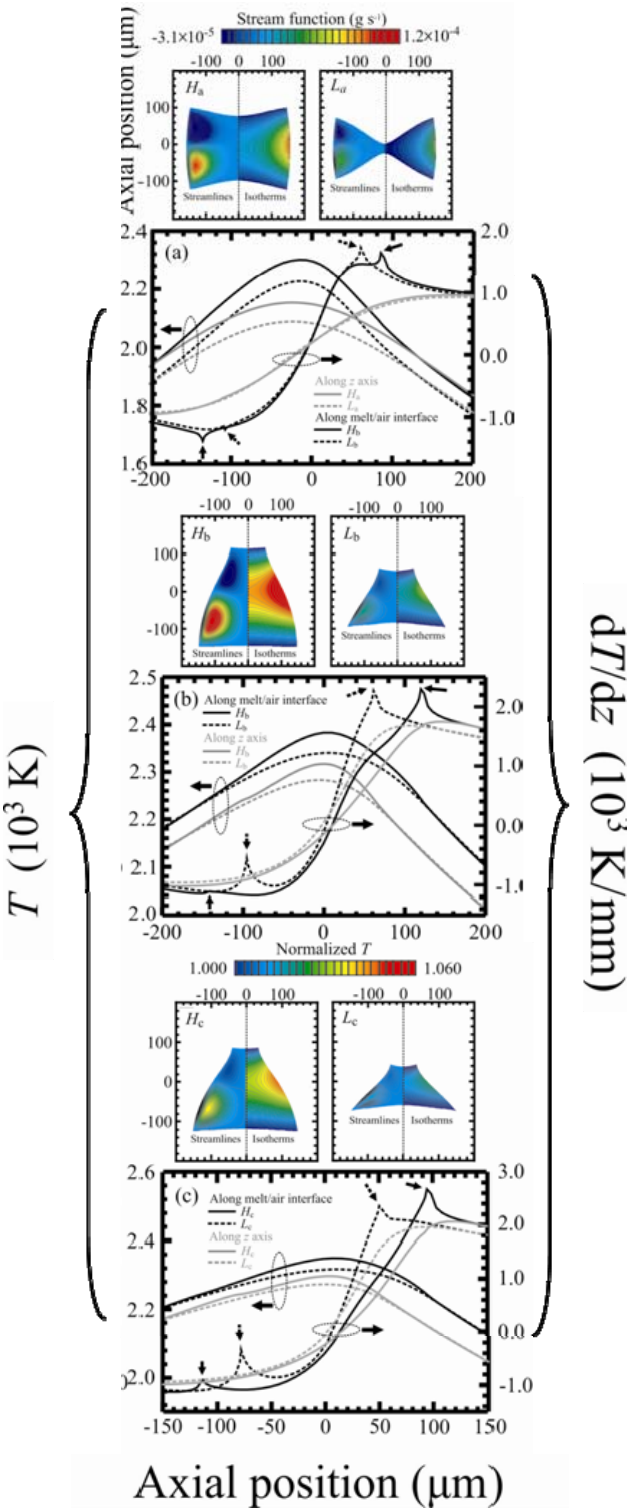

FIG. 4. T and dT/dz near the miniature MZs at various axial positions for different reduction ratios when operating at H and L power. The upper diagrams are corresponding streamlines and isotherms of miniature MZs.

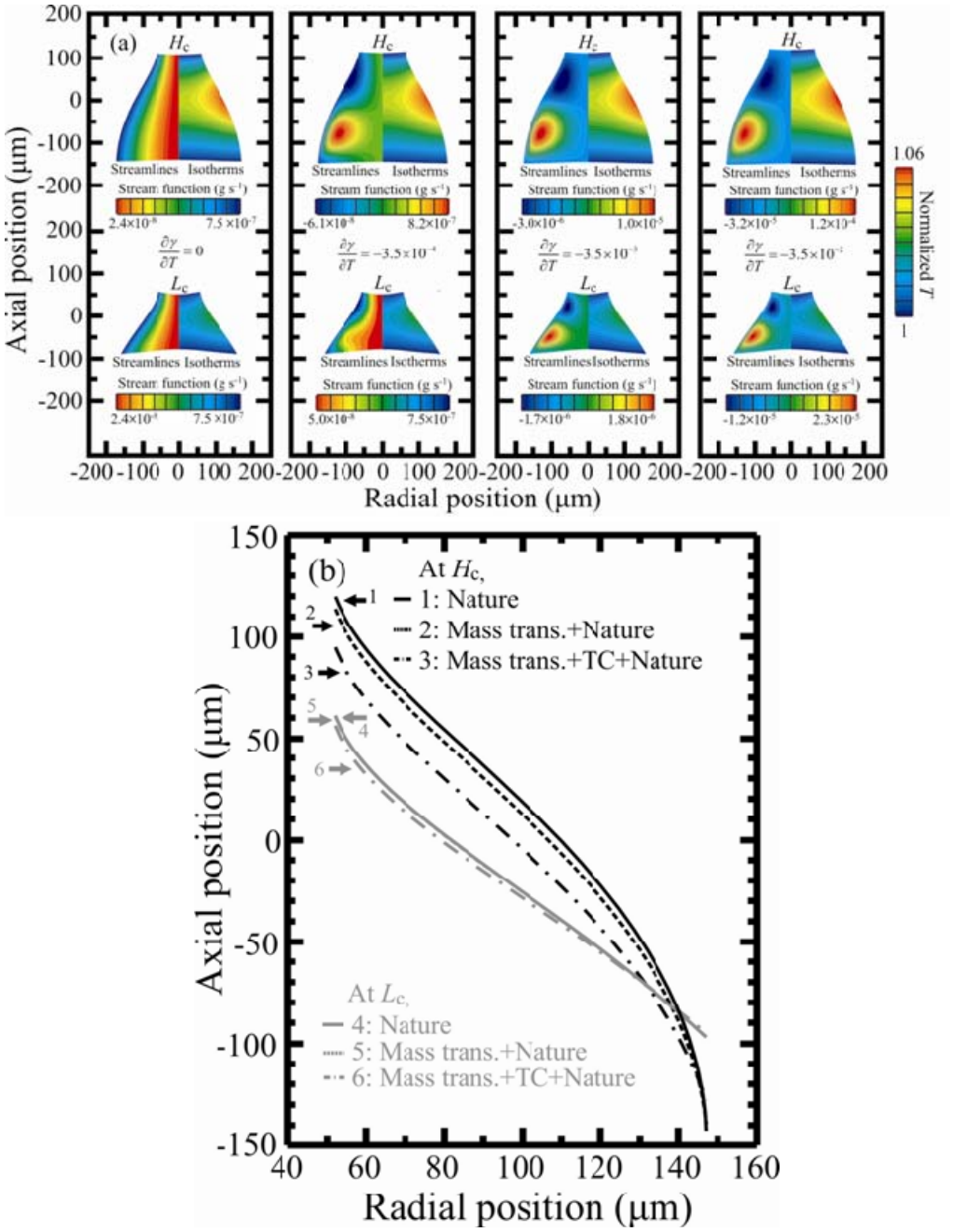

FIG.5. (a) the streamlines and isotherms for different $\partial\gamma/\partial T$, and (b) the radial positions of the melt/air interface at various axial positions by involving different kinds of thermal convections with the reduction ratio of 35%.